Laser surface modification of medical grade alloys for reduced heating in a magnetic resonance imaging environment

O. Benafan,[1,a),b)] S.-Y. Chen,[2] A. Kar,[2] and R. Vaidyanathan[1,b)]

[1]*Advanced Materials Processing and Analysis Center (AMPAC), Materials Science and Engineering, Mechanical and Aerospace Engineering, University of Central Florida, Orlando, Florida 32816, USA*
[2]*Laser-Advanced Materials Processing Laboratory, Center for Research and Education in Optics and Lasers (CREOL), College of Optics and Photonics, University of Central Florida, Orlando, Florida 32816, USA*

Nanoscale surface modification of medical grade metallic alloys was conducted using a neodymium-doped yttrium aluminum garnet laser-based dopant diffusion technique. The objective of this approach was to minimize the induction heating by reducing the absorbed radio frequency field. Such an approach is advantageous in that the dopant is diffused into the alloy and is not susceptible to detachment or spallation as would an externally applied coating, and is expected to not deteriorate the mechanical and electrical properties of the base alloy or device. Experiments were conducted using a controlled environment laser system with the ability to control laser properties (i.e., laser power, spot size, and irradiation time) and dopant characteristics (i.e., temperature, concentration, and pressure). The reflective and transmissive properties of both the doped and untreated samples were measured in a radio frequency (63.86 MHz) magnetic field using a system comprising a high power signal generator, a localized magnetic field source and sensor, and a signal analyzer. The results indicate an increase in the reflectivity of the laser-treated samples compared to untreated samples. The effect of reflectivity on the heating of the alloys is investigated through a mathematical model incorporating Maxwell's equations and heat conduction. © 2015 AIP Publishing LLC. [http://dx.doi.org/10.1063/1.4936970]

I. INTRODUCTION

Magnetic resonance imaging (MRI) has become a widely used imaging technique in medical diagnostics of the human body. MRI is a safe, noninvasive clinical procedure with non-ionizing radiation exposure unlike traditional x-rays or computed tomography (CT) scans. In a current clinical environment, a MRI system typically uses (i) static magnetic fields ranging from 0.2 to 3 tesla (T),[1,2] (ii) pulsed electromagnetic gradient field with pulsed intensities from 20 to 100 T/s, and (iii) radio frequency (RF) electromagnetic field with a frequency of 42.58 MHz/T and pulse peak amplitudes of ~14 μT.[3] These fields are used to construct images of tissue inside the human body, which provide reliable and often lifesaving diagnoses. However, exposure to these fields for patients with implanted metallic devices poses potential safety hazards, which prevent millions of patients worldwide from this imaging modality.[4,5] One such hazard is tissue heating in the vicinity of the metallic implant/device due to induction heating of the alloy by the pulsed RF magnetic field.[6] Thermal injuries at the metal-tissue interface have been identified as detrimental to patients wearing such devices, with greatest heating effects at the ends of implanted lead wire electrode. In some cases, a temperature rise from 26 to 74 °C was reported after 30 s of resonating RF waves around intravascular guide wires.[7] In other cases, a temperature rise of about 0.5 °C was measured for a stent exposed to the RF of a 1.5 T MRI

birdcage coil at 64 MHz.[8] Examples of other devices are cardiac pacemakers, implantable cardiac defibrillators (ICDs), deep brain stimulators (DBSs), endovascular coiling, stents, catheters, and drug pumps, amongst others.

Reducing the induced heating has been a topic of research for many years. *In vitro* and *in vivo* numerical and experimental studies have been conducted to address MRI related heating in implants and surrounding tissue.[5,9,10] Limiting a MRI procedure to lower specific absorption rates (SARs), body extremities away from the implant, or changing device position and lead path configuration (e.g., critical length and winding) have all been considered as possibilities to reduce the heating. While these possibilities have showed a noticeably reduced temperature rise, further improvements are still an absolute necessity. The objective of this work is to report on a laser surface medication technique[11–13] and measurements of the electromagnetic response of medical grade metallic alloys. To the best of the authors' knowledge, this is the first time such an approach is used in addressing MRI related heating.[12–14] The presented laser-based dopant diffusion technique is advantageous in that the implanted alloy is directly surface-treated to reduce the power deposited into it during a MRI sequence. Diffusion into the material is not susceptible to detachment or spallation as would be the case in an externally applied coating, and is expected to not deteriorate the mechanical and electrical properties of the base alloy or device. By tailoring the electromagnetic properties at the surface of the material, both the RF field coupling to the lead or device and the currents induced during the RF transmission can be reduced if not completely eliminated. Flat thin foils (25 μm thick and up) and wires with diameters as small as 100 μm of Ti, Ta, and MP35N® (SPS

---

a)Present address: Materials and Structures Division, NASA Glenn Research Center, Cleveland, Ohio 44135, USA.
b)Electronic addresses: othmane.benafan@nasa.gov and raj@ucf.edu

86, 123903-1

Technologies) were treated. As no off-the-shelf equipment was available, the measurement setup was uniquely assembled to measure the electromagnetic properties at frequencies matching the RF field frequencies (e.g., 63.86 and 127.74 MHz for 1.5 and 3 T static magnetic flux density, respectively). Since there is a direct correlation between the electromagnetic properties of materials and temperature rise, measurements of electromagnetic properties, i.e., incident, reflected, and transmitted magnetic flux density of both the laser-treated and as-received samples, are reported. Complementary characterization techniques were also used to investigate the materials' surface morphology and composition before and after laser treatment. Scanning electron microscopy (SEM) and energy-dispersive X-ray spectroscopy (EDS) were used for that purpose.

In addition to experimental and measurement techniques, electromagnetic and thermal models were developed for two purposes. The first was to determine the choice of dopant to be diffused into the alloy, taking into account the operational conditions and the materials under investigation. The second was to determine the effect of reflectivity/transmissivity on heating and temperature distribution in metallic implants during RF magnetic field pulses. Detailed descriptions of the laser diffusion method, measurement system, and results are presented in Secs. II, III, and V, respectively.

II. LASER DIFFUSION SYSTEM

The laser diffusion system was used for surface treating medical grade metallic alloys with the objective of reducing RF-induced heating during clinical MRI procedures. Although alloy treatments have been performed in typical heat treating furnaces, the laser diffusion method is advantageous in that the localized control over several parameters (e.g., variable dopant concentration, isolated treatment areas, skin depth, and patterns) otherwise impractical in a furnace was made possible. The laser diffusion system[11,15] consisted of three main sub-assemblies: (a) laser source, (b) sample environment, and (c) control/monitoring unit as shown in Fig. 1.

The laser source is a solid-state, lamp-pumped laser (LEE Laser, Inc., Model-8150MQ) with an 8–200 W output power

mounted on an optical rail. The lasing medium consisted of a Nd:YAG (neodymium-doped yttrium aluminum garnet, $Nd:Y_3Al_5O_{12}$) crystal operated in a continuous wave mode of wavelength $\lambda = 1064$ nm. On the optical rail, a low power Helium-Neon (HeNe) continuous laser was used for sample alignment on the chamber. The laser sub-assembly is composed of a highly reflective rear mirror, laser head which houses the lamps and the crystal, cavity, shutter and indicators, transmissive front mirror or output mirror, aperture, bending mirror, and a focusing system. Since the laser system was stationary on the rails, the only varied parameters on the laser system were the laser power controlled from the power station and the focusing lens. The laser power, used as a localized heating source, was varied according to the material under test considering both the material (e.g., Ti, Ta, or MP35N) and geometry (e.g., foils, sheet, or wire). Before each experiment, the laser power at the sample surface was measured using a hand-held power meter (PW-250, SYNRAD, Inc.).

The material to be treated was placed inside a vacuum chamber which made up the sample environment sub-assembly. The sub-assembly consisted of the vacuum chamber, bubbler, heater, and x-y-z stage (Fig. 1). The vacuum chamber used was a three port, 304 stainless steel chamber with a pressure range of 10^{-7} to 2500 mbar and a temperature range of -196 to 300 °C. The sample was placed inside the chamber on a positioning block centered on the beam line. One port was used for the vacuum system (a mechanical roughing and diffusion pump) which produced a desired vacuum of approximately 1.3×10^{-6} bars. In line with the vacuum system port, a digital pressure gauge was used for pressure measurements and monitoring. A dial pressure gauge was also used in the second port of the chamber for a secondary pressure measurement point. The third and last port was connected to a precursor-containing bubbler. The precursor used in the laser doping experiments was platinum (II) acetylacetonate ($C_{10}H_{14}O_4Pt$) dissolved in acetylacetone ($C_5H_8O_2$) as described in Sec. IV and elsewhere.[12] The precursor was heated in the bubbler to 130 °C using a heater and type-K thermocouples for temperature measurements. Once the precursor was evaporated, argon carrier gas was
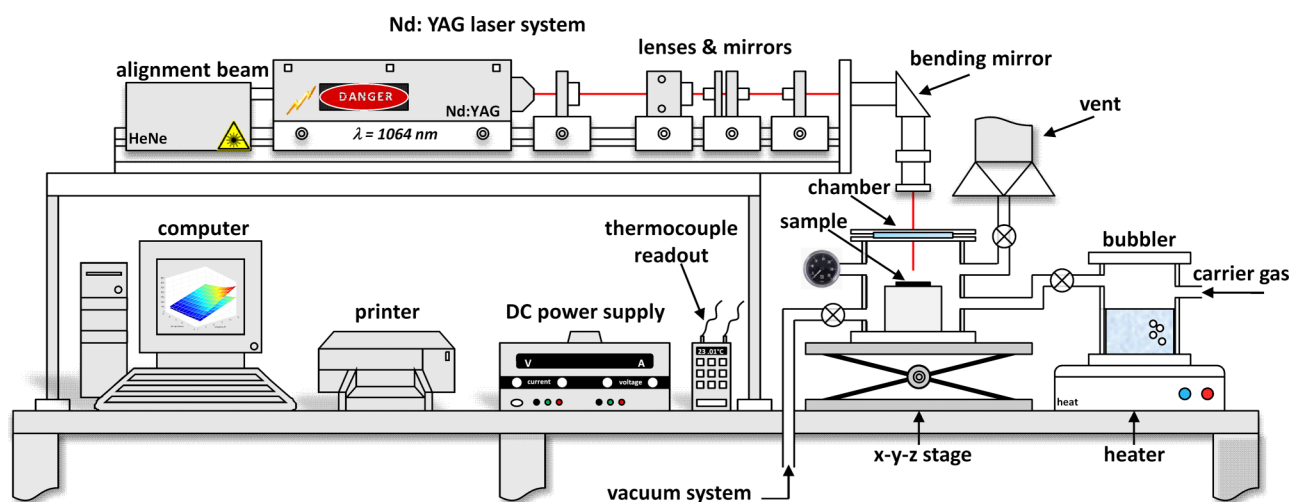

FIG. 1. Experimental setup of the Nd:YAG laser diffusion system.

passed through the bubbler to transport the vapor to the doping chamber with a backfill pressure of 1.034 bars. In conjunction with the laser heated surface of the material, the precursor decomposed and produced platinum atoms which then diffused into the material surface.

For safety purposes, a vent line was tapped into the line connecting the chamber and bubbler, which served the dual purpose of venting the excess vapor at the end of each experiment, and pressure relief in case of over pressurization. The last component of the sample environment sub-assembly was the x-y-z stage. The x-y stage movement was automated using two uni-slides and two VXM stepper motor controllers (Vexta PK266-03A-P1, Velmex, Inc.) with 400 steps per revolution and 3.175 μm advance per step, while the -z-stage translation was adjusted manually using an intermediate laboratory jack (Fig. 2). Since the laser beam was stationary, the desired laser exposure on the sample was achieved by controlling the x-y stage translation. Laser parameters such as the laser beam size and focal length were adjusted using the z-stage, while the dwell time, scanning speed, and areas of exposure were controlled from the x-y stage. It is noted here that since the laser beam is stationary, the scanning speed is obtained by adjusting the stage movement speed.

The control and monitoring sub-assembly consisted of a computer, printer, DC power supply, and temperature readouts. Automated control over the translation stages helped maintain constant stage speed and uniform laser exposure throughout the sample. In addition, consistency from one sample to the next in terms of laser exposure and treated areas was achieved

with such automation. Precursor temperature was monitored from both the heater display and thermocouple readouts. This duplication in temperature measurement was essential since evaporation of the precursor at 130 °C is of primary importance for effective laser diffusion treatment. Although not presented in this work, the laser beam profile using different lenses was also measured using a pyroelectric solid-state array camera (Pyrocam™I, Ophir-Spiricon, Inc.).

The three sub-assemblies described above worked together to allow laser surface-treating of medical grade alloys. High purity Ti, Ta, and MP35N alloy foils ranging from 25 to 150 μm thick were treated with the aforementioned laser diffusion setup. Laser exposure on different foils was varied by the scanning speed of the translation stages (Table I).

The same laser setup was modified for elongated wire treatment as shown in Fig. 2. The vacuum system port was modified using a cross adapter to accommodate the vacuum line, bubbler line, pressure gauge, and safety vent on the same port. For continuous wire drawing and laser treatment, two spools, one with metallic wire and the other initially empty, were placed on holders at opposing sides of the chamber (Fig. 2). The wire feed spool (wire spool) was free to rotate on the holder, while the wire winding spool (initially empty spool) was connected to an electric DC motor at the rotation stage powered by the power supply shown in Fig. 1. In this case the x-y stage was not moved, and only the stage rotation was controlled for appropriate height and speed. Two custom-built wire feedthroughs were connected on two opposing ports of the sample chamber. These feedthroughs allowed for
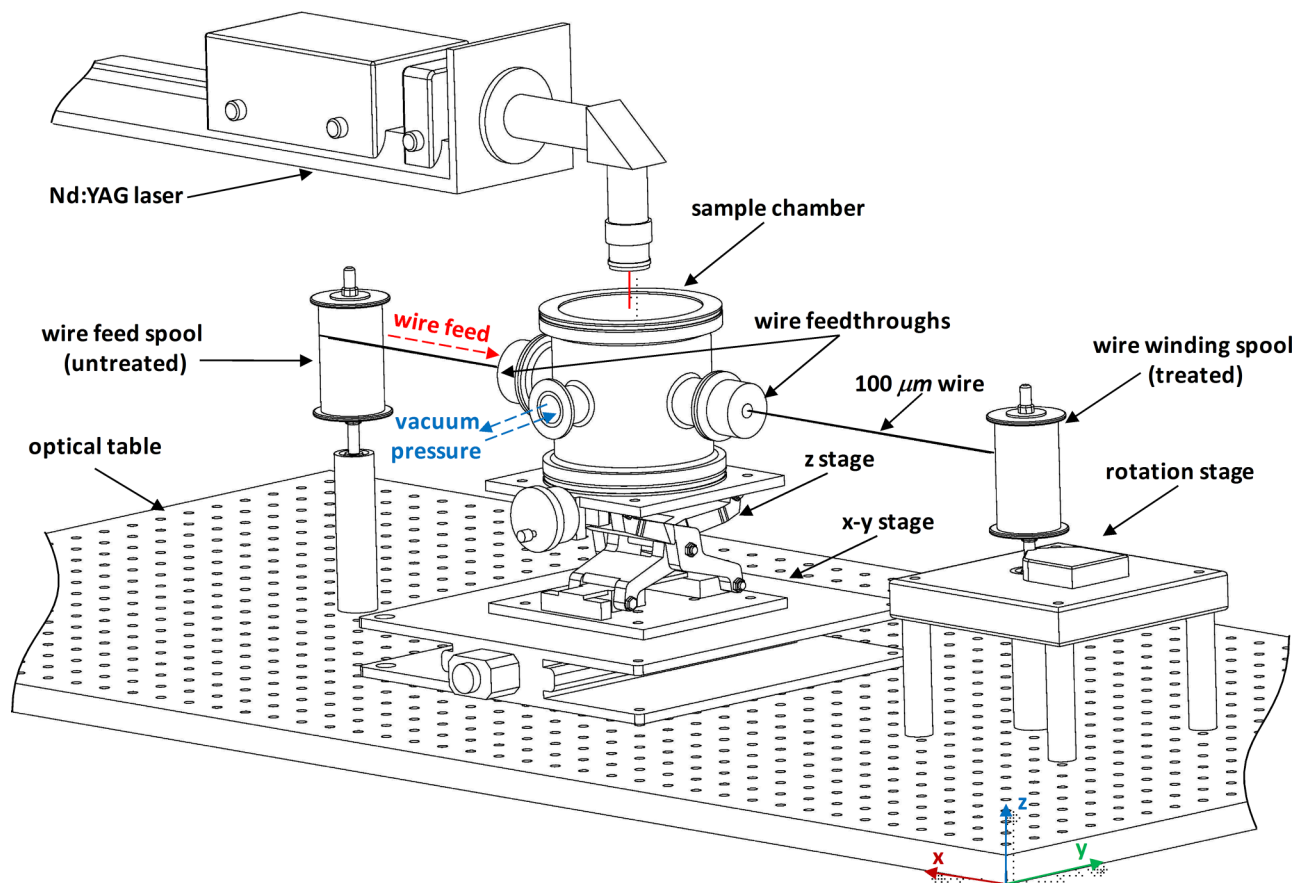

FIG. 2. Modified laser diffusion setup for continuous wire doping.

TABLE I. Laser processing parameters for MP35N, Ta, and Ti in both sheet and wire forms.

Material	Dopant		Laser power (W)		Scanning speed (mm/s)		Backfill pressure (bar)		Laser passes (#)		Beam radius (μm)	
	Sheet	Wire	Sheet	Wire	Sheet	Wire	Sheet	Wire	Sheet	Wire	Sheet	Wire
MP35N	$C_{10}H_{14}O_4Pt$		3.5	3–7	2	8–11	1.034	1.034	1–3	1	403	420
Ta	+		3.5	3–9	2	8	1.034	1.034	1–3	1	403	420
Ti	$C_5H_8O_2$		3.5–5	…	2	…	1.034	…	1–3	…	403	…

pressure/vacuum sealing and wire feeding for laser treatment. Leakage was measured using a helium mass spectrometer and was found to approximately $\sim 10^{-5}$ cm^3/s leakage flow in dynamic conditions, i.e., while moving the wire through the chamber. This minimal leakage rate was negligible for the application in hand since a spool of wire treatment did not last more than 1 h. For different wire drawing speeds and wire diameters, it is conceivable that the leak rates may change and should be verified. The feedthroughs also allowed for adjusting the wire tension by opening or closing the access orifice. This way, there was no reduction in wire diameter during the wire treatment and drawing. Using this modified doping setup, continuous laser treatment of wires with diameters as small as 100 μm and ~ 6 m long was accomplished. The benefit of this continuous laser doping was that the treated wires could then be directly made into medical leads (e.g., cardiac leads, DBS leads, catheters) with the ultimate goal of reduced heating during a MRI procedure.

III. MAGNETIC FIELD SYSTEM

The overall goal of the magnetic field system was to measure the magnetic properties of the as received samples (untreated) and after their treatment using the laser diffusion system described above. These measurements directly relate to the temperature rise of the alloys through appropriate modeling efforts using Maxwell's and thermal equations. The construction of a suitable magnetic field measurement system was governed by the following requirements and constraints.

(i)   Measurement frequency (f): The magnetic field measurements were to be conducted at a RF electromagnetic field frequency of 63.86 MHz for a 1.5 T static magnetic flux density (B_0). Associated with this RF field are the heating effects caused by the induced currents and magnetic induction.[16] A system was required to generate these fields to replicate representative MRI operating conditions.

(ii) RF magnetic field (B_1): Pulse peak amplitude of ~ 14 μT was needed to represent the magnitude of the RF magnetic field. This amplitude was required to be applied to planar samples with a cross section of 20×20 mm^2 (treated and untreated samples). Conventional loops or Helmholtz coils were not suitable due to the size of the hardware compared to the small specimen being investigated.

(iii) Reflectivity and transmission modes: Both reflectivity and transmission measurements were required to assess the RF induced heating through modeling efforts. The

setup needed to allow for varying the incident field angle and shielding.

With these requirements and challenges in mind, several measurement techniques were attempted before developing the final magnetic field system. For the frequency and amplitude considered, there was no readily available equipment to carry out these measurements. The first measurement attempted was based on a transmission line method. This setup consisted of a RF signal generator, vector network analyzer, waveguides and coaxial airlines, and a computer. The samples were placed inside the waveguide or coaxial airline perpendicular to the long axis that filled the entire cross section. The receiver was tuned to the RF frequency (63.86 MHz) to detect the reflected and transmitted signal from the material. However, unstable and unrepeatable measurements were obtained caused by the imperfections of the sample (gaps between the wall of the waveguide and sample), non-magnetic nature of the samples used, and foil thickness insensitivity. In addition, the RF magnetic field peak amplitude was less than 1 nT. The second method consisted of an impedance material analyzer based on a contacting electrode method. The measurements were performed in open and short circuit compensation at the specified frequency. As with the first method, inconsistencies and instabilities were unavoidable due to the high electrical conductivity of the material and low magnetic field outputs.

The measurement method used in this work consisted of a non-contacting, non-destructive free space method. This method is widely used for high frequency applications and more so for much larger samples than the 20×20 mm samples used in this work.[17,18] As a result, the free space measurement setup was customized to fit the application in hand. The magnetic field setup consisted of a signal generator, magnetic field source and sensor, signal analyzer, and positioning fixtures as shown in Fig. 3. The RF fields were generated at 63.86 MHz by a RF analog signal generator (MXG-AT-N5181A, Agilent Technologies) with a high power output option. No external amplifier was used in this case since high power was directly produced from the generator's electronic attenuator. The output from the generator was connected to a localized magnetic field source (AT-11940A, Agilent Technologies) through a RG-223 coaxial cable and adapters. The magnetic field generated was measured using a close-field probe (labeled magnetic field source in Fig. 3), electromagnetic sensor (HP 11940A, Hewlett Packard) connected to a pre-amplified spectrum analyzer (AT-N9320B/PA3, Agilent Technologies). The close field-probe sensor was used since only the radiated magnetic field produces an output signal
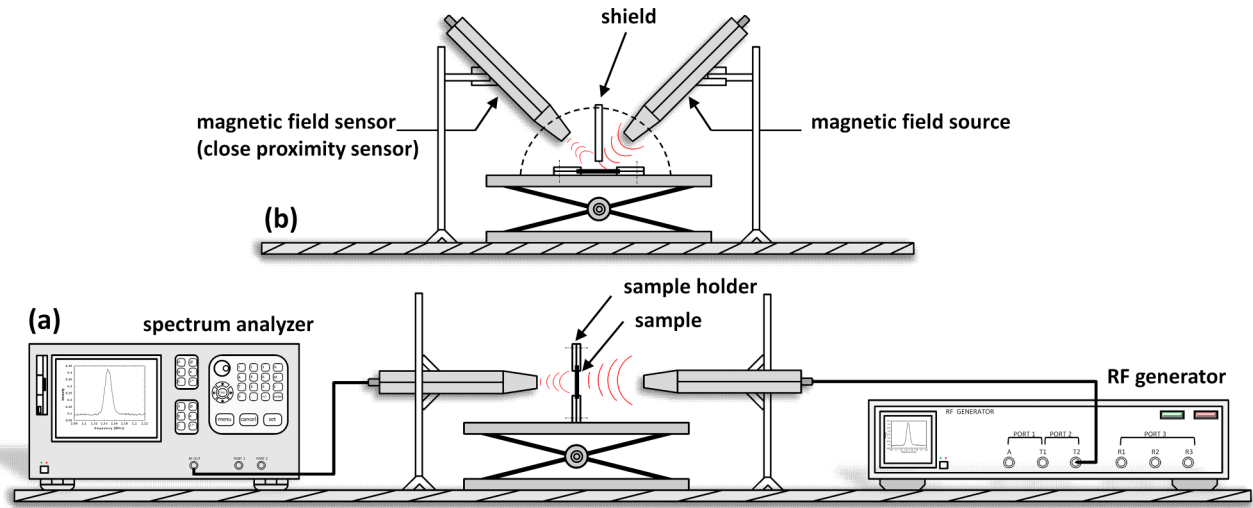
FIG. 3. Magnetic field system for measurement in (a) transmission mode and (b) reflection mode.

while the electric field does not due to the dual-loop sensors and balun used in the probe tip construction.

Vertical stands and clamps were used to adjust the magnetic source and sensor angles for transmission (Fig. 3(a)) and reflectivity (Fig. 3(b)) measurements of 20×20 mm^2 samples ranging from 25 to 150 μm thick. The rectangular samples were placed on a sample holder positioned on a z-stage for alignment purposes. This sample holder was made large enough so that no radiation propagates around the holder edges and results in erroneous measurements. In the reflectivity measurement mode, a shield was used between the source and sensor to avoid direct field coupling between the source and sensor probes.

IV. ELECTROMAGNETIC AND THERMAL MODELS

Modeling efforts centered on developing electromagnetic and thermal models for the purpose of identifying the appropriate dopant and temperature rise due to the magnetic field interaction with the material. The behavior of the electric and magnetic waves is described by Maxwell's equations, and along with the constitutive relations, the electromagnetic field interaction with the material can be completely described.[12,13] The following one-dimensional governing equation in the Cartesian coordinate is used in this analysis:[19]

$$\frac{\partial^2 B_z(x,t)}{\partial x^2} = \mu\varepsilon\frac{\partial^2 B_z(x,t)}{\partial t^2} + \mu\sigma\frac{\partial B_z(x,t)}{\partial t} \text{ for x > 0, } (1)$$

where B_z is the magnetic flux density, μ is the permeability, ε is the permittivity, and σ is the electrical conductivity. In the case of conductive materials, the displacement current density (first term in the left hand side of Eq. (1)) is much smaller than the conductive current density (second term in the left hand side of Eq. (1)) which can be neglected to yield the diffusion equation. Applying the boundary conditions $B_z(0,t) = B_0 \sin(\omega t), B_z(\infty,t) = 0$ and initial condition $B_z(x,0) = 0$, the steady state solution was determined to be

$$B_z(x,t) = B_0 e^{\left(-\frac{x}{\delta}\right)} \sin\left(\omega t - \frac{x}{\delta}\right), \delta = \sqrt{\frac{2}{\omega\mu\sigma}}, \quad (2)$$

where ω is the angular frequency and δ is the skin depth. This solution was used with different material properties to determine the magnetic flux density inside the material. Ti, Ta, Au, Ag, Cu, and Pt were all modeled and their corresponding response as a function of skin depth is shown in Fig. 4. The choice of dopant was based on the material with the least magnetic field penetration, i.e., less absorbed energy which implies reduced heating. Ti and Ta were used as a reference material to determine the appropriate dopant with a superior magnetic field response. Copper was shown to be the material with the least magnetic field penetration; however, it was ruled out due to biocompatibility issues.[20] Gold and silver as base metals were also found to exhibit a low field penetration, but the material cost is high. This led us to the choice of platinum as a starting dopant. From several platinum precursors, for example, trimethyl (methylcyclopentadienyl) platinum ($C_9H_{16}Pt$), dimethyl platinum cyclooctadiene, and platinum (II) acetylacetonate ($C_{10}H_{14}O_4Pt$), the latter was deemed the better because of its low vaporization and thermochemical decomposition temperatures.[13]
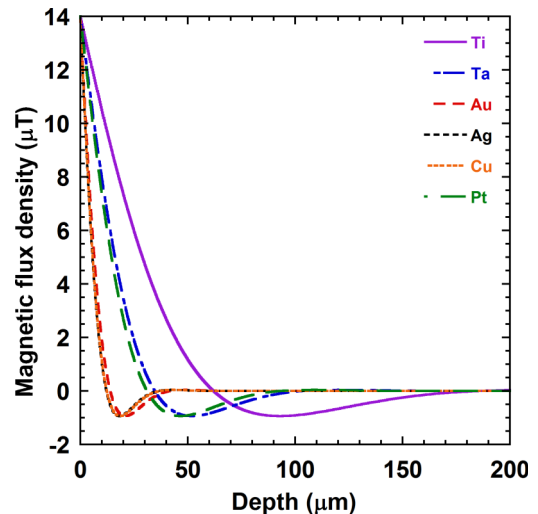

FIG. 4. Magnetic field penetration in different metals used for dopant selection (model predictions using Eqs. (1) and (2)).

The simplified thermal model was developed to determine the temperature distribution due to the incident RF magnetic pulses. The model accounted for heat conduction, volumetric heat generation rate, and convection surface conditions based on the energy conservation given by the following one-dimensional heat conduction equation in the Cartesian coordinate:[21]

$$k \frac{\partial^2 T(x,t)}{\partial x^2} - \frac{\partial \bar{S}(x,t)}{\partial x} = \rho \cdot C_p \frac{\partial T(x,t)}{\partial t}, \quad (3)$$

where k is the thermal conductivity, ρ is the mass density, C_p is the specific heat, and $\bar{S}$ is the time-average Poynting vector as determined from the electromagnetic model. The terms on the right hand side of Eq. (3) are the net conduction heat flux entering the material and the rate of thermal energy generation due to the RF pulses. The term on the right hand side corresponds to the rate of thermal energy stored within the material. The boundary and initial conditions are given by

$$k \frac{\partial T(x,t)}{\partial x}\bigg|_{x=0} = h \left(T(x,t) - T_\infty \right)\big|_{x=0}, \quad (4a)$$

$$k \frac{\partial T(x,t)}{\partial x}\bigg|_{x=l} = h \left(T_\infty - T(x,t) \right)\big|_{x=l}, \quad (4b)$$

$$T(x,0) = T_i = T_\infty, \quad (4c)$$

where h is the heat transfer coefficient and T_i and T_∞ are the initial and surrounding temperatures, respectively. Eq. (3) was then solved with the imposed conditions of Eq. (4). A representative relationship between the temperature difference and the reflectivity based on the solution of Eq. (3) is shown in Fig. 5 for Ti. These results were obtained considering the RF pulse repetition rates (50–175 Hz) and time (30–60 s), pulse magnitude of 14 μT, and an average heat transfer coefficient ranging from 1 to 100 W/m² · K. As the reflectivity increases, the temperature rise decreases since less energy is absorbed by the implanted lead or device. The model predictions for all materials showed similar trends in the temperature rise. The reflectivity and transmission data are now measured for the untreated and treated samples.
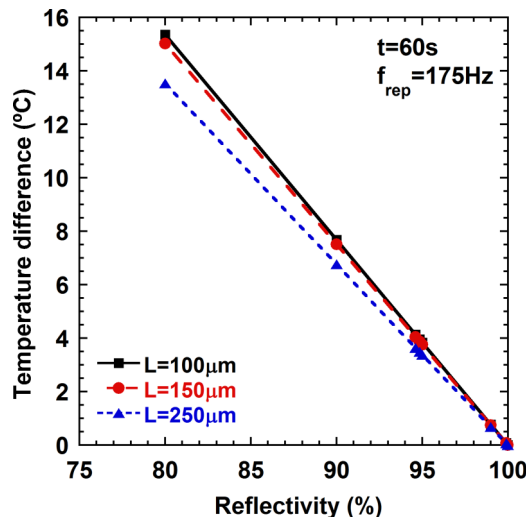
FIG. 5. Relationship between the temperature difference and the reflectivity for Pt-doped titanium with different thicknesses (model predictions using Eq. (3)).
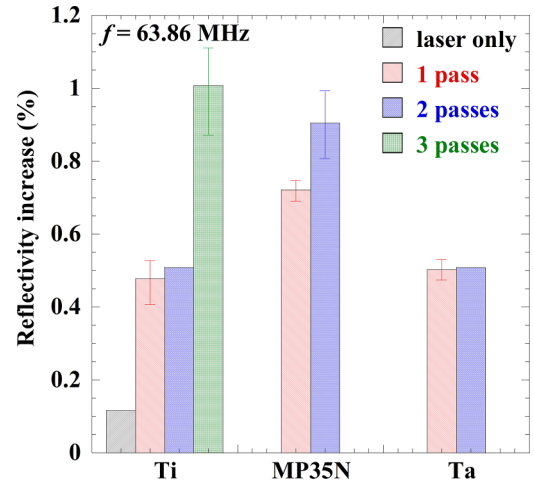
FIG. 6. Reflectivity measurements with respect to the untreated material for Ti, MP35N, and Ta at 63.86 MHz and a laser power of 3.5 W. The error bars represent data obtained from multiple measurements.

V. EXPERIMENTAL RESULTS

Using the laser diffusion setup and the values listed in Table I, thin Ti, Ta, and MP35N foils were surface treated. Optimization of the laser parameters was obtained analytically and for the most part experimentally by varying the laser power, sample environment, backfill pressure, scanning speed, laser beam size, precursor concentration and temperature, irradiation time, and number of laser passes. Figure 6 shows reflectivity measurements with respect to the untreated material for Ti, MP35N, and Ta at a RF frequency of 63.86 MHz. These quantities were obtained by first measuring the magnetic flux density derived using[22]

$$B(\mu T) = 10^{\left[\frac{V(dB \mu V) + \Gamma(dB((\mu A/m)/\mu V)) + K(dB)}{20} \right]} \cdot \mu_o(\mathrm{H/m}), \quad (5)$$

where $V(\mathrm{dB}\ \mu\mathrm{V})$ is the measured voltage on the spectrum analyzer, $\Gamma(\mathrm{dB}((\mu\mathrm{A/m})/\mu\mathrm{V}))$ is the probe antenna factor, K (dB) is the loss or gain between the probes and the instrument, and $\mu_o = 4\pi 10^{-7}$ H/m is the permeability of free space. For the frequency and coaxial cables used, the antenna factor was measured to be 48.5 dB $((\mu\mathrm{A/m})/\mu\mathrm{V})$ and the gain was found to be ± 2 dB. The reflectivity increase plotted in Fig. 6 was then determined using

$$R_{increase} = \frac{R_{treated} - R_{as-received}}{R_{as-received}} \times 100. \quad (6)$$

It is important to note that these measurements were obtained using a low magnetic flux density of 0.3 μT due to the instrument limitation. All four laser treatments of 250 μm thick samples, i.e., laser only with different laser passes, showed an increase in reflectivity compared to the as-received samples. The increase of the laser only treatment can be due to localized amorphization at the laser-material interface. Treatment with platinum dopant during laser passes also showed an increase which is primarily attributed to the platinum doping. The doping served to alter the electrical conductivity since platinum has a higher conductivity of $\sigma_{pt} \approx 9.66 \times 10^6$ m⁻¹ Ω⁻¹ compared to 2.34×10^6, 0.97×10^6, and 7.61×10^6 m⁻¹ Ω⁻¹ for Ti, MP35N, and Ta, respectively.[23] Measurements of the
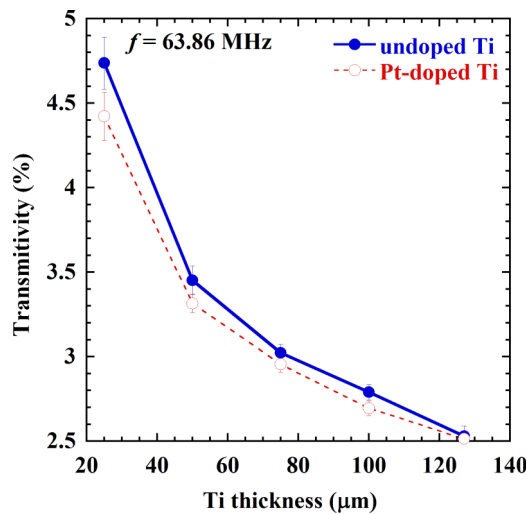
FIG. 7. Transmitivity measurements of undoped (as-received) and Pt-doped Ti sheets at 63.86 MHz. No transmission was detected for Ti thicknesses above 127 μm.

transmitted field were also obtained for different Ti thicknesses as shown in Fig. 7. As expected, the reflectivity decreases with increasing sample thickness up to 127 μm where no transmitted field was detected. In all sample thicknesses, the transmission through the treated samples (open symbols of Fig. 7) was lower than that through the as-received, untreated samples (solid symbols of Fig. 7). Although the changes are small, the decreasing trend throughout multiple thicknesses is an indication that the electromagnetic properties of the material were altered. It was determined that the energy deposited in Ti foils was reduced by 4.2% which directly related to a temperature decrease from Eq. (3).

Thin wires (100 μm in diameter) were also treated using the setup of Fig. 2. A parametric study on the effect of different environments, laser powers, and dopant concentration on the surface of wires was made. For these wires, initial parameters such as scanning speed and laser power were determined using surface maps as shown in Fig. 8. These surface maps, plotted for Ta and MP35N wires, represent the relationship between local temperatures, wire speed, and laser power. Low speeds
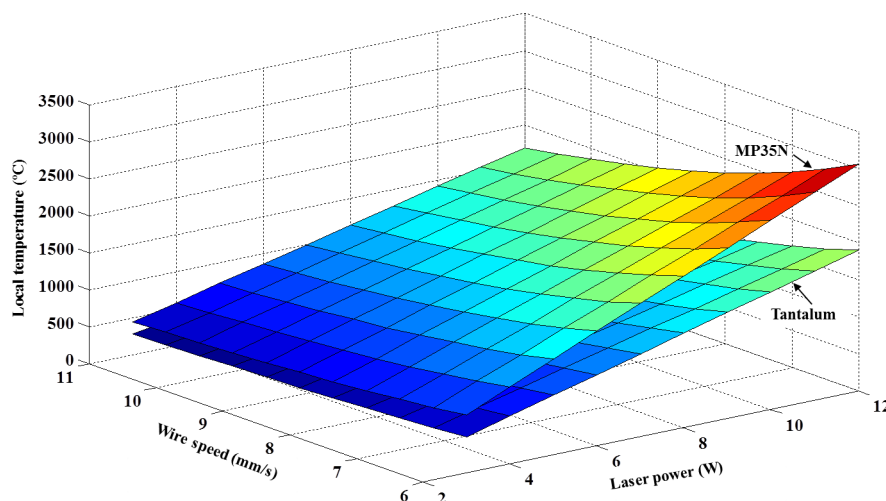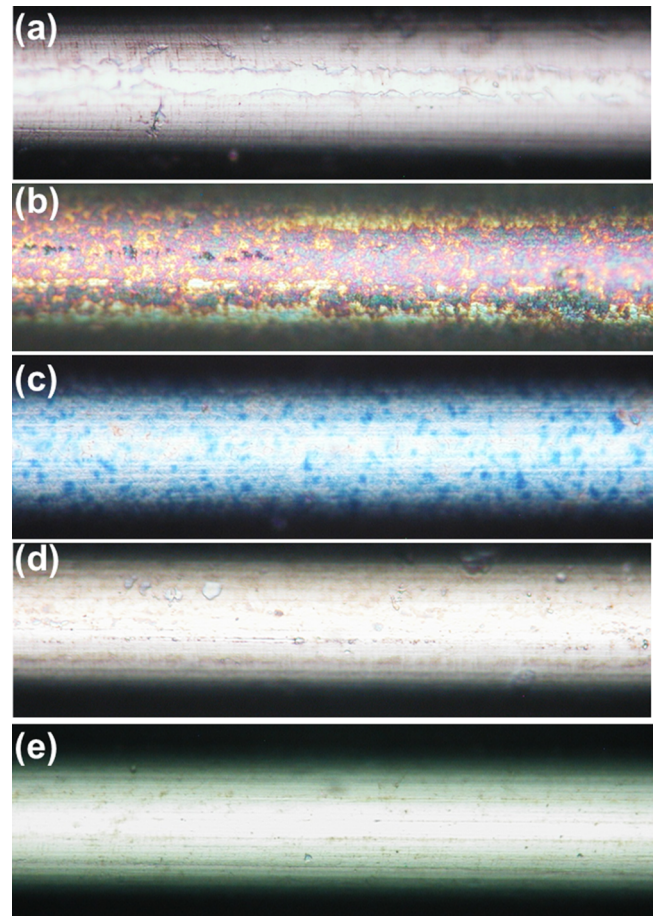

FIG. 9. Optical micrographs of MP35N wires (100 μm) treated in different environments. (a) As received, (b) air, (c) vacuum, (d) argon, and (e) Pt-doped. The experiments were conducted using a laser power of 3 W, a scanning speed of 8 mm/s, and a laser beam radius of 420 μm.

and high laser powers resulted in very high local temperatures which will yield and break the material during the wire processing and drawing. Once the processing parameters were finalized, the environment effects while processing in air, vacuum, argon, and platinum were assessed. Fig. 9 shows an example of MP35N optical micrographs using the same

FIG. 8. Surface maps of local temperature, wire speed, and laser power of Ta and MP35N wires (100 μm) used for selection of laser processing parameters.
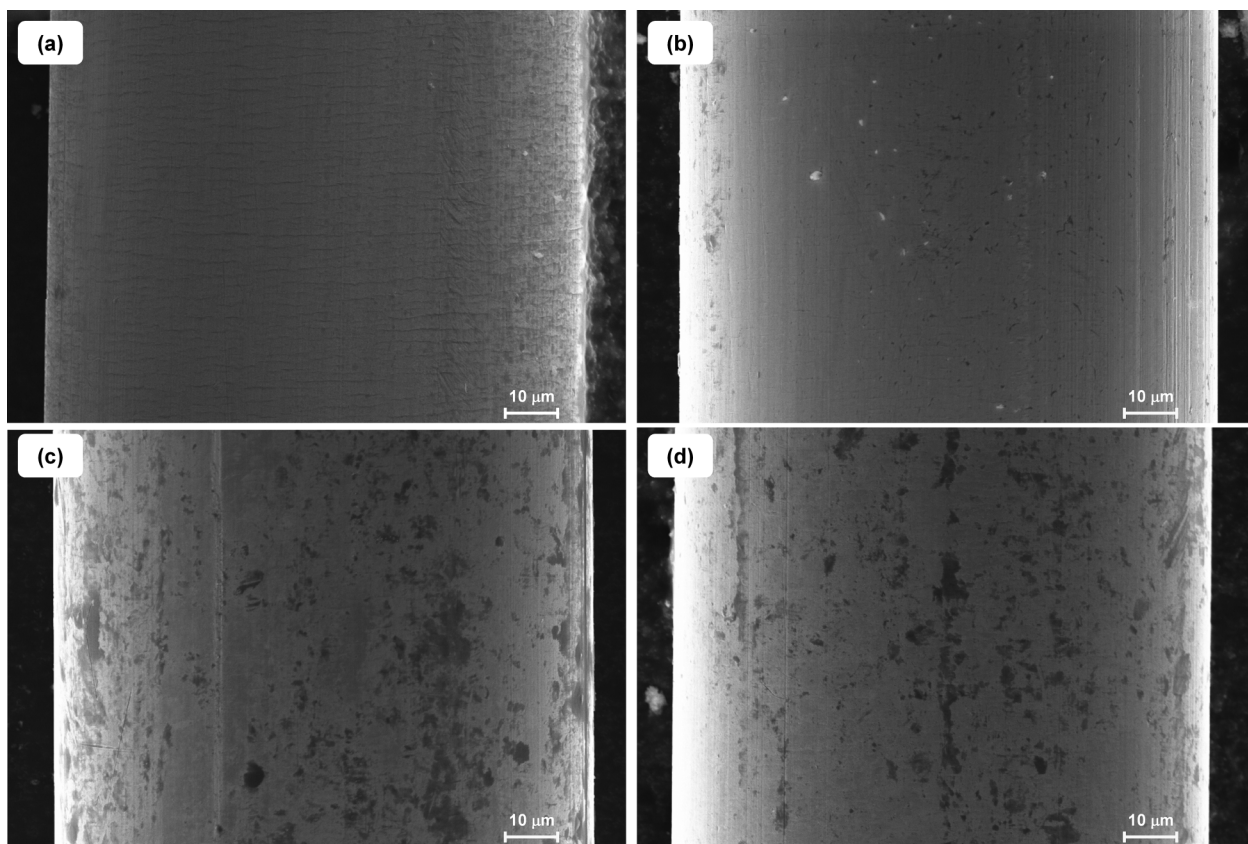
FIG. 10. SEM images of MP35N wires treated with different laser powers. (a) As-received and Pt-doped using a laser power of (b) 3 W, (c) 5 W, and (d) 7 W.

laser parameters, i.e., same speed, power, beam size, and focal length. The wires treated in air and vacuum show significant oxidation compared to the as-received wire sample. Processing in argon gas seemed not to alter the surface, and similarities can be observed. The final treatment in a platinum environment showed an improved surface with less cracks and defects when compared to the as-received wire.

The laser power effects were also evaluated. In this case, all wires were treated under the same environment while the laser power was increased. Representative secondary electron SEM images of the as-received and treated MP35N wires are shown in Fig. 10. These images were obtained using a Zeiss ULTRA-55 FEG SEM (Carl Zeiss NTS, LLC) at 1 K magnification with an extra high tension (EHT) of
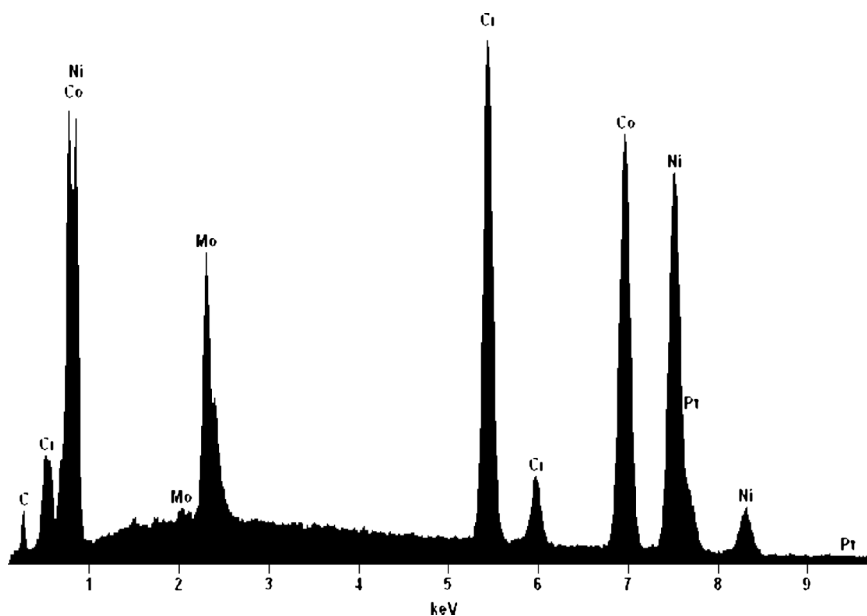

FIG. 11. Energy-dispersive X-ray spectrum of Pt-doped MP35N wire. The processing conditions consisted of a laser power of 3 W, a scanning speed of 8 mm/s, and a laser beam radius of 420 μm.

15 kV. Notice the improvements in the surface morphology as previously described. The surface cracks (Fig. 10(a)) that were introduced during the wire drawing of the as-received material were removed after processing with the platinum precursor. The effect of increasing laser power on the surface is shown in Figs. 10(c) and 10(d) by the dark features on the surface for a laser power of 5 and 7 W, respectively. These features are believed to be oxides that form on the surface during the processing and drawing stage. It was further verified with the SEM that the features are not pits or cavities on the surface.

Energy-dispersive X-ray spectroscopy was used to quantify the platinum volume fraction on the doped wires. Fig. 11 shows a representative spectrum of a Pt-doped MP35N wire treated at 3 W with evidence of platinum at 9.44 keV. The volume fractions were found to be 0.06, 0.17, and 0.08 ± 0.02 at. % for 3, 5, and 7 W, respectively. The spectrum also contained traces of carbon at 0.282 keV which was transferred to the sample from the vacuum feedthroughs. Variation of the laser power helped to identify the optimum treatment which yielded a good surface finish and suitable platinum composition for reduced heating.

VI. SUMMARY

A laser diffusion experimental setup and a magnetic field measurement system were successfully assembled and evaluated for nanoscale surface modification of medical grade metallic alloys. The deposition of a platinum precursor, selected using an electromagnetic model, was shown to alter the electromagnetic properties of the treated alloys which directly relate to reduced MRI related heating as assessed using simplified thermal models. Measurements of reflectivity and transmissivity using the low magnetic field system showed an increase in reflectivity and decrease in energy deposition. Continuous laser treatment of both thin foils and wires showed surface improvements in addition to reduced heating. This laser diffusion method can be applied to treating many implanted leads and devices such as cardiac pacemakers and defibrillators with the goal of reducing the RF induced heating. This method has the potential for partnering where devices or alloys can be treated in complex forms. Future system improvements include the use of laser beam shaping through lens design to avoid effect of overlapping laser passes and

modification of laser irradiance distribution. A high magnetic flux density system with RF pulse amplitudes of 14 μT is also under development for the measurements of electromagnetic properties at high field magnitudes. In addition, refined thermal and electromagnetic models that account for more variables and dimensions are being devised. Measurements of mechanical properties and temperature rise are also sought in future tasks.

[1]D. L. Price, J. P. De Wilde, A. M. Papadaki, J. S. Curran, and R. I. Kitney, J. Magn. Reson. Imaging **13**(2), 288 (2001).
[2]J. F. Schenck, J. Magn. Reson. Imaging **12**, 2 (2000).
[3]F. G. Shellock, *Magnetic Resonance Procedures: Health Effects and Safety* (CRC Press, Boca Raton, FL, 2001).
[4]M. F. Dempsey, B. Condon, and D. M. Hadley, J. Magn. Reson. Imaging **13**, 627 (2001).
[5]E. Mattei, M. Triventi, G. Calcagnini, F. Censi, W. Kainz, G. Mendoza, H. I. Hassen, and P. Bartolini, BioMed. Eng. OnLine **7**(1), 11 (2008).
[6]F. G. Shellock, J. Magn. Reson. Imaging **12**, 30 (2000).
[7]M. K. Konings, L. W. Bartels, H. F. Smits, and C. J. Bakker, J. Magn. Reson. Imaging **12**(1), 79 (2000).
[8]H. Bassen, W. Kainz, G. Mendoza, and T. Kellom, Minim. Invasive Ther. Allied Technol. **15**(2), 76 (2006).
[9]J. A. Nyenhuis, S.-M. Park, R. Kamondetdacha, A. Amjad, F. G. Shellock, and A. R. Rezai, IEEE Trans. Device Mater. Reliab. **5**, 467 (2005).
[10]M. T. Marshall, K. K. Liao, M. K. Loushin, and P. A. Iaizzo, PACE **33**, 826 (2010).
[11]S. Bet, N. R. Quick, and A. Kar, Acta Mater. **56**, 1857 (2008).
[12]S.-Y. Chen, O. Benafan, R. Vaidyanathan, and A. Kar, Opt. Lasers Eng. **62**, 132 (2014).
[13]S.-Y. Chen, O. Benafan, R. Vaidyanathan, and A. Kar, Appl. Phys. A **116**, 703 (2014).
[14]R. Vaidyanathan and S. C. Larsson, U.S. patent No. 8,644,951 (4 February 2014).
[15]G. Lim and A. Kar, Mater. Sci. Eng., B **176**, 660 (2011).
[16]R. Buchli, P. Boesiger, and D. Meier, Magn. Reson. Med. **7**, 255 (1988).
[17]D. K. Ghodgaonkar, V. V. Varadan, and V. K. Varadan, IEEE Trans. Instrum. Meas. **37**(3), 789 (1989).
[18]F. Zaki, Z. Awang, N. H. Baba, A. S. Zoolfakar, R. Abu bakar, M. Zolkapli, and N. Fadzlina, in Proceedings of 2010 IEEE Student Conference on Research and Development (SCOReD 2010), Putrajaya, Malaysia, 13-14 December 2010.
[19]P. A. Bottomley and E. R. Andrew, Phys. Med. Biol. **23**(4), 630 (1978).
[20]M. Gosau, M. Haupt, S. Thude, M. Strowitzki, B. Schminke, and R. Buergers, "Antimicrobial effect and biocompatibility of novel metallic nanocrystalline implant coatings," J. Biomed. Mater. Res., Part B (published online).
[21]M. R. Hossan, D. Byun, and P. Dutta, Int. J. Heat Mass Transfer **53**(5), 5129 (2010).
[22]M. Terrien, "The 11940A close field probe: Characteristics and application to EMI troubleshooting," in RF and Microwave Measurement Symposium and Exhibition, July 2004.
[23]See http://www.matweb.com/search/PropertySarch.aspx for a listing of electrical conductivities.